nature communications

Article

https://doi.org/10.1038/s41467-025-56580-9

A high-entropy alloy showing gigapascal superelastic stress and nearly temperature-independent modulus

Received: 26 April 2024

Accepted: 20 January 2025

Published online: 31 January 2025

Check for updates

Junming Gou[1,5] ✉, Guoxin Liu[1,5], Tianzi Yang[1], Xiaolian Liu[2], Yun Pan[1], Chang Liu[3], Yu Qian[1], Yao Liu[1], Ying Chen[1], Xuefeng Zhang[2], Tianyu Ma[1] ✉ & Xiaobing Ren[4]

High-performance superelastic materials with a combination of high superelastic stress, large elastic recovery strain, and stable elastic modulus over a wide temperature range are highly desired for a variety of technological applications. Unfortunately, it is difficult to achieve these multi-functionalities simultaneously because most superelastic materials have to encounter the modulus softening effect and the limited superelastic stress, whereas most Elinvar-type materials show small elastic strain limit. Here, we report a $(TiZrHf)_{44}Ni_{25}Cu_{15}Co_{10}Nb_6$ high-entropy alloy that meets all these requirements. This alloy also shows good cyclic stability, thermally-stable capacity for elastic energy storage, high micro-hardness and good corrosion resistance, allowing it to operate stably in hostile environments. We show that its multi-functionalities stem from a natural composite microstructure, containing a highly-distorted matrix phase with strain glass transition and various structural and compositional heterogeneities from micro- to nano-scale. Our findings may provide insight into designing high-entropy alloys with unconventional and technologically-important functional properties.

Lightweight, miniaturization and precision design for industrial and space applications poses a big challenge for superelastic materials, which need not only to possess high superelastic stress (σ_C, the critical stress to induce long-range martensitic transformation) and large elastic recovery strain (ε_E, the elastically recovered component of recovery strain), as illustrated in the inset of Fig. 1a, but also able to maintain stable elastic modulus over a wide temperature range (known as Elinvar effect)[1–3]. On the one hand, when deformed to a fixed strain, the capability of elastic energy storage (or the elastic energy stored per unit volume $E_{elastic} = \int_{\varepsilon_{rem}}^{\varepsilon_{max}} \sigma(\varepsilon)d\varepsilon$, as illustrated in Supplementary Fig. S1)[4,5] for a high-σ_C superelastic material is usually superior to that for a low-σ_C one, hence storing a fixed elastic energy required a smaller volume of high-σ_C superelastic material. Large hysteresis can be easily induced by small external stress in low-σ_C superelastic materials, leading to the sensitivity deterioration, precision loss and fatigue damage[6]. In addition, under a fixed external force, the higher σ_C a superelastic material has, the smaller volume it is required to achieve a desirable recovery strain. On the other hand, the stable and precise operation of elastic devices also requires temperature-independent elastic modulus and large ε_E[1,5]. For example, the suspension system of Mars/lunar rover may require the combination of all these functional properties. Due to the mutually-exclusive principles, materials with the combination of all these properties are still rare, thus unsatisfying the superelastic applications[7,8].

[1]Frontier Institute of Science and Technology, and State Key Laboratory for Mechanical Behavior of Materials, Xi'an Jiaotong University, Xi'an 710049, China. [2]Institute of Advanced Magnetic Materials, College of Materials and Environmental Engineering, Hangzhou Dianzi University, Hangzhou 310012, China. [3]College of Materials Science and Engineering, Sichuan University, Chengdu 610065, China. [4]Center for Functional Materials, National Institute for Materials Science, Tsukuba 305-0047, Japan. [5]These authors contributed equally: Junming Gou, Guoxin Liu. ✉e-mail: goujunming@xjtu.edu.cn; matianyu@xjtu.edu.cn

https://doi.org/10.1038/s41467-025-56580-9

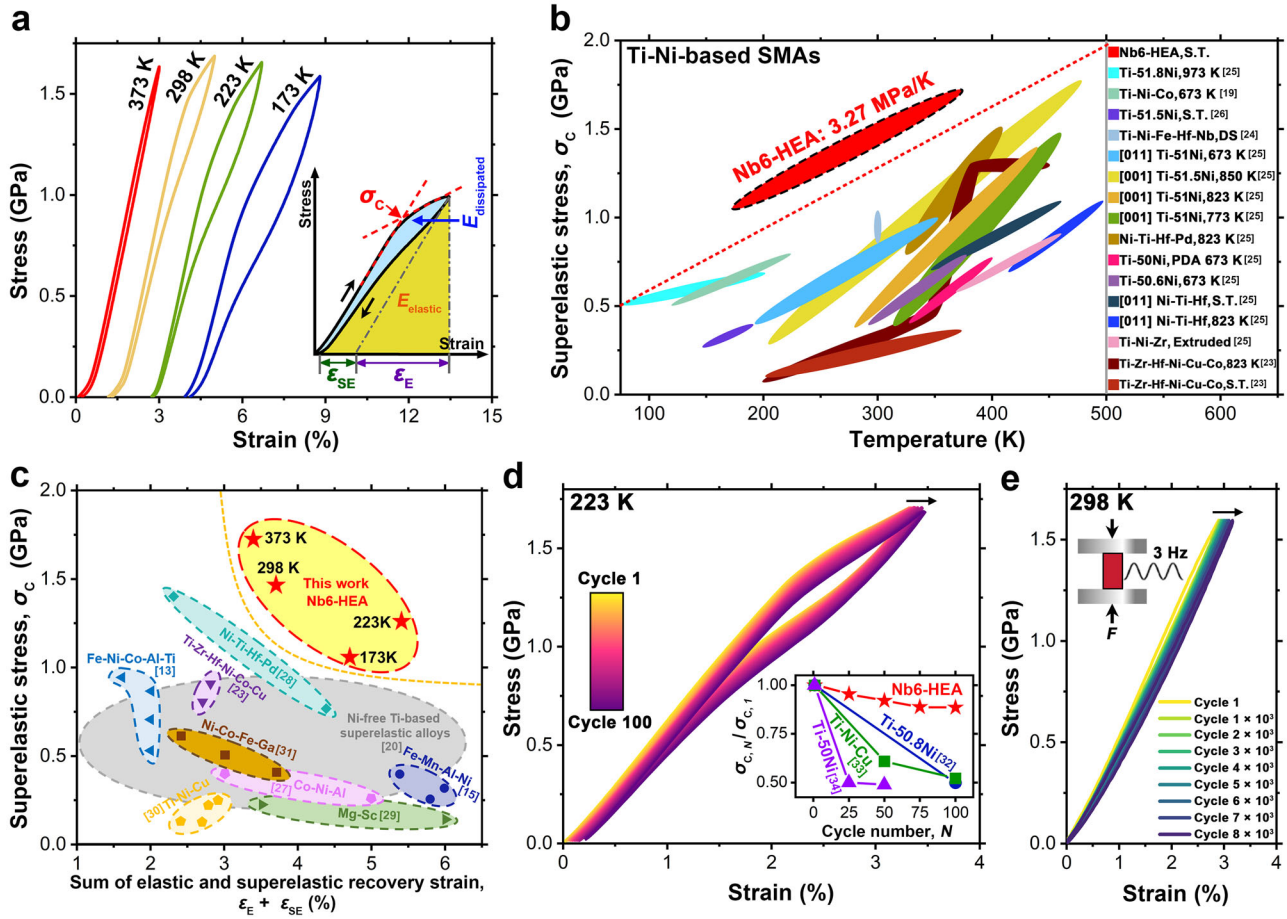

Fig. 1 | Superelastic property and cyclic performance of Nb6-HEA. **a** Temperature-dependent compressive superelastic responses of Nb6-HEA, and the inset is the illustration for the superelastic stress σ_C determined by the tangent method[19,20], the elastic recovery strain ε_E (i.e., the elastically recovered component of recovery strain) and the superelastic recovery strain ε_{SE} (i.e., the superelastically recovered component of recovery strain)[21], the elastic energy $E_{elastic}$ and the dissipated energy $E_{dissipated}$. **b** Temperature-dependent σ_C of Nb6-HEA and landmark Ti-Ni-based shape memory alloys (SMAs)[19,23–26], where the ovals are meant to contain ranges of data points for different alloys. S.T. stands for solution treatment, DS stands for directional solidification, and PDA stands for post-deformation annealing. **c** The superelastic stress σ_C versus the sum of elastic and superelastic recovery strain (i.e., $\varepsilon_E + \varepsilon_{SE}$) of Nb6-HEA and its comparison with conventional superelastic materials[13,15,20,23,27–31]. **d** Cyclic compressive stress-strain curves of Nb6-HEA measured at 223 K, under a constant applied stress of 1.7 GPa, and the inset shows the ratio of $\sigma_{C,N}$ to $\sigma_{C,1}$ ($\sigma_{C,N}$ is σ_C at the N^{th} cycle, $\sigma_{C,1}$ is σ_C at the first cycle) of Nb6-HEA as a function of cycle number N, and its comparison with Ti-50Ni, Ti-50.8Ni and Ti-36Ni-13Cu SMAs[32–34]. **e** Room-temperature fatigue test of the Nb6-HEA, performed under a constant applied stress of 1.6 GPa with frequency of 3 Hz, in the compressive mode (as illustrated in the inset).

Strong atomic bonding in bulk metallic materials can ensure a high strength, but the elastic strain limit is usually less than 1%[1]. Besides, the ever-present cooling-strengthened bonding always leads to an elastic modulus hardening effect[9]. Whilst the shape memory alloys (SMAs) with stress-induced martensitic transformation (SIMT), such as Ti-Ni-[8], iron-[10] and Cu-based[11] alloys, can exhibit the superelastic recovery strain ε_{SE} larger than 8%, but their soft lattice nature makes a low σ_C, usually less than 1 GPa[3]. Typically, the conventional SMAs exhibit superelasticity within a limited temperature range[12], for example, it is about 232-284 K for Ti-50.6Ni alloy[8], and about 193–298 K for Fe-Ni-Co-Al-Ti alloy[13]. Below this temperature range, martensite becomes thermodynamically stable, thus engendering shape memory effect; above this temperature range, σ_C for overcoming the energy barrier of SIMT will exceed the yield strength of austenite, leading to undesirable plastic deformation. In addition, σ_C of conventional SMAs usually decreases upon cooling, following the Clausius-Clapeyron relation[14]. For example, the temperature dependence of σ_C in Ti-50Ni alloy is about 6 MPa/K[15], which will lead to a narrow temperature range for high σ_C. Despite that wide temperature range of superelasticity can be achieved in Fe-Mn-Al-Ni alloy (77-513 K) by the assist of magnetic contribution to the Gibbs energies[15] and in Co-Cr-based Heusler alloy (10–373 K) with reentrant martensitic transformation[16], high σ_C is still difficult to achieve, e.g., σ_C is lower than 0.6 GPa in Fe-Mn-Al-Ni alloy and 0.9 GPa in Co-Cr-based Heusler alloy. Moreover, these martensitic alloys inevitably suffer the elastic modulus softening effect due to the thermally-induced phase instability[7], thus mismatching the Elinvar requirement. Consequently, the intrinsic trade-off between superelastic stress and the temperature sensitivity of elastic modulus preclude the combination of wide-temperature-range high-σ_C superelasticity and Elinvar effect in conventional superelastic alloys.

Recently, wide-temperature-range superelasticity has been achieved in the alloys without a thermoelastic martensitic transformation, e.g., in defects-carrying Ti-Ni-based alloys with strain glass transition (a short-range strain ordering with decreasing temperature)[17] and Ni-Co-Fe-Ga alloy at supercritical state[18]. In addition, the strain glass transition can also compensate for the ever-present modulus hardening effect, thus giving rise to nearly temperature-independent low modulus, as reported in Mg-Sc alloys[5]. Although the stress-induced phase transformation at nano-scale or a continuous phase transformation in these alloys can expand the temperature range and reduce the intrinsic hysteresis of conventional

martensitic alloys, they still exhibit the same drawbacks as other superelastic alloys, and their soft lattice nature still prevents the achievement of high σ_C. Therefore, the achievement of wide-temperature-range high-σ_C superelasticity and stable elastic modulus still needs a new strategy.

In this work, we report a high-entropy alloy (HEA) $(TiZrHf)_{44}Ni_{25}Cu_{15}Co_{10}Nb_6$ (named as the Nb6-HEA) that exhibits a good combination of ultrahigh superelastic stress, large elastic recovery strain, and Elinvar effect over a wide temperature range. Detailed investigations revealed that these mutually-exclusive properties were achieved by a composite microstructure, where the constituting compositional variation separates this alloy into the highly-distorted matrix phase with a strain glass transition and the randomly-distributed non-transforming heterogeneities (varying in size, structure and composition). The interactions between the matrix and various heterogeneities give rise to ultrahigh-σ_C superelasticity with weak temperature dependence; the continuous lattice softening effect of the transformative matrix also compensates for the ever-present elastic hardening of non-transforming heterogeneities, thus yielding nearly temperature independent elastic modulus. This study suggests that the manipulating of multiple compositional and structural components in HEAs are appealing for developing high-performance functional materials.

Results

Superelastic response and stability

Figure 1a shows the temperature-dependent compressive superelastic responses of Nb6-HEA, which are obtained under a high stress level over 1.6 GPa. This alloy possesses both high superelastic stress σ_C and large elastic recovery strain ε_E over a wide temperature range from 373 K down to 173 K (see details in Supplementary Fig. S2). For comparison, conventional tangent method[19,20] is utilized to determine σ_C (i.e., σ_C is the corresponding stress for the intersection point of two tangents in the loading stress-strain curve), and the elastic recovery strain ε_E and superelastic recovery strain ε_{SE} are distinguished according to previous literature[21], as illustrated in the inset of Fig. 1a. At 373 K, this alloy exhibits a nearly non-hysteretic linear deformation with ε_E (or elastic strain limit) up to 3%, much larger than that of conventional metals and alloys[22], and ultrahigh σ_C of 1.72 GPa. At room temperature (298 K), it shows a quasi-linear superelastic response with high σ_C of 1.46 GPa, large ε_E of 2.5% and small ε_{SE} of 1.2%. At 223 K, it can exhibit large ε_E of 2.5% and modest ε_{SE} of 2.9%, and its sum of ε_E and ε_{SE} (i.e., $\varepsilon_E + \varepsilon_{SE}$) is comparable with that of polycrystalline Ti-Ni alloys[8]. More importantly, its σ_C is 1.26 GPa at 223 K, much higher than that of Ti-50Ni alloy (σ_C is about 0.25 GPa at 223 K)[15]. At 173 K, it still maintains high σ_C over 1 GPa, which was technologically challenging in traditional shape memory alloys (SMAs). As shown in Fig. 1b, the Nb6-HEA shows a wider temperature range for high σ_C, in comparison with landmark Ti-Ni-based SMAs[19,23–26]. It also exhibits relatively weaker temperature dependence of σ_C (3.27 MPa/K) than Ti-50Ni alloy (5.7 MPa/K) and Ti-Nb alloy (4.4 MPa/K), comparable with Fe-Ni-Co-Al-Ta-B alloy (3.1 MPa/K)[15]. Despite that high σ_C can be achieved in Ti-Ni-based SMAs at elevated temperatures, it will rapidly decrease below 1 GPa when cooling to room temperature. The trade-off between high σ_C and large $\varepsilon_E + \varepsilon_{SE}$ is also overcome in the present Nb6-HEA, which are superior to conventional superelastic alloys, such as iron-, Co-, Ti-Ni-, Ni-free Ti-based and recently-found high-entropy SMAs[13,15,20,23,27–31], as shown in Fig. 1c.

Conventionally, σ_C of traditional SMAs will decrease rapidly after several loading-unloading cycles, which is harmful for operating repeatedly[32,33]. For example, σ_C decreases from 0.6 GPa to 0.3 GPa after 100 cycles in Ti-50.8Ni alloy[32]; and σ_C decreases from 0.23 GPa to 0.12 GPa after 100 cycles in Ti-36Ni-13Cu alloy[33]. As shown in Fig. 1d, despite that the Nb6-HEA exhibits stress hysteresis at 223 K, it possesses high σ_C (>1.2 GPa) after 100 cycles, and its ε_E and ε_{SE} are nearly unchanged. In this alloy, the cycling-induced deterioration of σ_C is much weaker than those in the landmark Ti-Ni-based SMAs (inset of Fig. 1d)[32–34]. Good cycling stability can also be obtained at its lower temperature limit 173 K, as shown in Supplementary Fig. S3. Figure 1e shows that the Nb6-HEA possesses a long fatigue life over more than 8×10^3 cycles at a high stress amplitude of 1.6 GPa, being comparable with the advanced $Ni_{35}Co_{20}Fe_{18}Ga_{27}$ superelastic alloy (8×10^3 cycles at 1.05 GPa)[18]. Conventionally, the lower stress amplitude is, the better cycling stability a superelastic material has[35]. Thus, a longer fatigue life of the Nb6-HEA would be expected, when decreasing the applied stress in engineering applications. At its upper temperature limit 373 K, this alloy also exhibits nearly-unchanged stress-strain response after 100 cycles (Supplementary Fig. S4a). Note that after exposing to 373 K for a long time (e.g., 10 days), σ_C of this alloy will show an improvement at the sacrifice of a modest reduction of $\varepsilon_E + \varepsilon_{SE}$ (Supplementary Figs. S4b and S4c), which could be resulted from the diffusion-driven precipitation, like the formation of isothermal ω nanoparticles in β-Ti alloys[36].

Temperature-insensitive modulus/elastic energy, micro-hardness and corrosion resistance

The Nb6-HEA also exhibits a nearly temperature-independent tensile modulus (Elinvar-type effect) over a wide temperature range from 323 K down to 173 K, determined from the corresponding tensile loading-unloading curves, as shown in Fig. 2a. By contrast, the commercial spring steel exhibits the normal elastic modulus hardening effect due to the thermally-induced weakness of anharmonic vibration, and the Ti-Ni alloy exhibits the elastic modulus softening effect that has been commonly observed in superelastic materials[7]. The average temperature coefficient of modulus $\bar{e}$ (i.e., $\Delta E/(E_0 \Delta T)$) is 6.14×10^{-5} K^{-1} from 198 K to 273 K, satisfying the criterion for Elinvar effect[1]. As shown in Supplementary Fig. S5a, under constant tensile stress of 400 MPa, the number of cycles to failure (N_f) of the Nb6-HEA is 6182. By lowering the tensile stress to 300 MPa, it can exhibit a better tensile cyclic stability over more than 10000 cycles (Supplementary Fig. S5b). Owing to its temperature-independent modulus and high σ_C, this alloy possesses thermally-stable high elastic energy $E_{elastic}$ (i.e., capability for elastic energy storage) over a wide temperature range, as shown in Fig. 2b. Notably, Elinvar-like behaviors have also been observed in some specific alloys (e.g., Ti-Ni-Co and Ti-Ni-Cu strain glass alloys[37,38]), which are determined by their weak temperature dependence of AC (i.e., storage) modulus under a very small stress/strain amplitude. One important difference here is that the present Nb6-HEA can show Elinvar effect under a high compressive stress of 600 MPa, being superior to the previously-reported strain glass alloys (as summarized in Supplementary Table S1). We have also prepared a Nb-free $(TiZrHf)_{50}Ni_{25}Co_{20}Cu_5$ HEA, which exhibits nearly temperature-independent AC modulus over a wide temperature range (Supplementary Fig. S6). Unfortunately, under high compressive stress, both of modulus and $E_{elastic}$ of this Nb-free HEA exhibits are highly sensitive to temperature (inset of Fig. 2b), hence unsatisfying the practical elastic applications at high stress level. Note that after exposing to its upper temperature limit 373 K for 10 days, the Nb6-HEA can still exhibit Elinvar effect over a wide temperature range (Supplementary Fig. S7).

When serving as the leaf spring in automobile, the suspension system in rover and biomedical guide wires, elastic materials are also required to possess high micro-hardness for resisting the surface scratch induced by sharp objects impinging in operation[39]. It is because the local stress concentration on the surface scratch can lead to the formation of micro-cracks under loading-unloading cycles, further resulting in undesirable fracture or fatigue damage[40]. As shown in Fig. 2c, the Nb6-HEA possesses higher micro-hardness than conventional structural materials (e.g., SUS316L stainless steels and Ti-Al-V alloys) and elastic materials (e.g., Ti-2448 and Ti-Ni-based alloys)[41–44]. In the biomedical applications[41] and ocean thermal energy harvesting[45],

https://doi.org/10.1038/s41467-025-56580-9

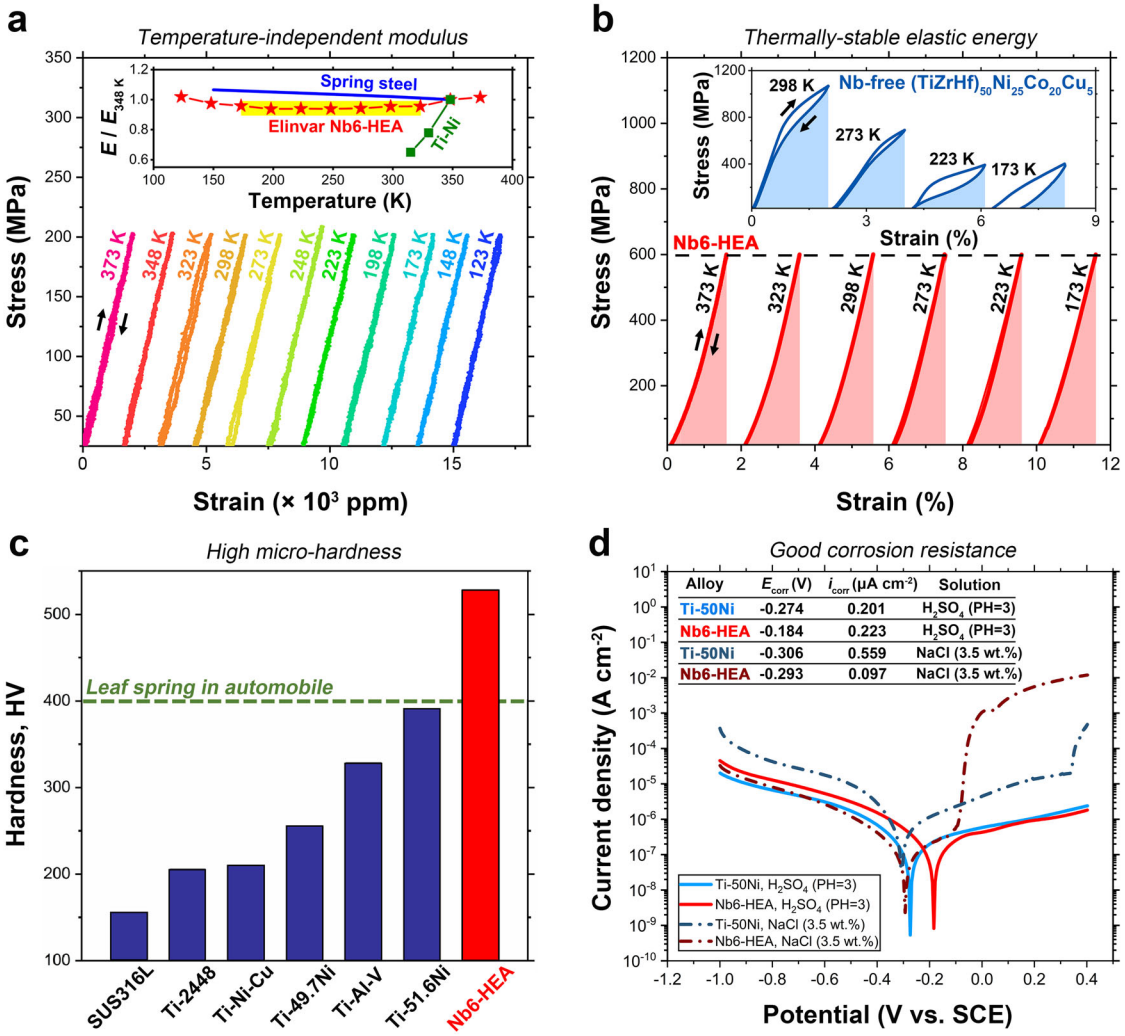

Fig. 2 | Multiple macroscopic properties of Nb6-HEA. a Tensile loading-unloading stress-strain curves of Nb6-HEA tested from 373 K down to 123 K, and inset shows that Nb6-HEA exhibits a nearly temperature-independent (Elinvar-type) modulus over the temperature range of 173–323 K (as indicated by the yellow shading), a behavior contrasting with the elastic modulus hardening of non-transforming spring steel and the elastic modulus softening of Ti-Ni martensitic alloy. **b** Compressive loading-unloading stress-strain curves of Nb6-HEA with applied stress of 600 MPa, showing thermally-stable non-hysteretic stress-strain response and elastic energy $E_{elastic}$ (shaded areas), contrasting with a Nb-free $(TiZrHf)_{50}Ni_{25}Co_{20}Cu_5$ HEA with strongly temperature-dependent elasticity (inset). **c** A comparison of micro-hardness between Nb6-HEA and conventional structural and elastic materials[41–44]. **d** Potential polarization curves of Nb6-HEA and Ti-50Ni alloy in NaCl (3.5 wt.%) solution and H_2SO_4 (PH = 3) solution, where E_{corr} is the corrosion potential, i_{corr} is the corrosion current density, and the reference electrode is Calomel electrode (SCE).

SMAs are also required to possess good corrosion resistance in hostile environments. As shown in Fig. 2d, in H_2SO_4 (PH = 3) solution, the corrosion potential E_{corr} of Nb6-HEA (-0.184 V) is higher than that of Ti-50Ni alloy (-0.274 V); in NaCl (3.5 wt.%) solution, the corrosion current density i_{corr} of Nb6-HEA (0.097 μA cm^{-2}) is much lower than that of Ti-50Ni alloy (0.559 μA cm^{-2}). These results suggest that the Nb6-HEA possesses high micro-hardness and good corrosion resistance simultaneously, like the advanced Co-Cr-Al-Cr SMAs[41].

Natural composite microstructure

Figure 3a shows the X-ray diffraction (XRD) pattern of Nb6-HEA, revealing a phase mixture of ordered body-centered-cubic (bcc) B2 matrix (a_{B2} = 0.312 nm) and a small volume fraction of β-Nb phase with disordered bcc A2 structure ($a_{β\text{-}Nb}$ = 0.331 nm). The lattice parameter of B2 matrix in this alloy is larger than that in Ti-50Ni binary alloy (a_{B2} = 0.3015 nm)[46], because its alloying of elements Zr, Hf have larger atomic radii than Ti, and Co, Cu have larger atomic radii than Ni. The inset energy dispersive spectrometer (EDS) mapping clearly displays micron-sized β-Nb secondary phase. Due to the lattice misfit between B2 matrix and β-Nb phase, Moiré fringe engendered by the local stress concentration can be observed at their interface (Supplementary Fig. S8). Notably, the $\{110\}_{B2}$ fundamental reflection (Fig. 3b) exhibits asymmetric contour, which can be decomposed into two isolated peaks by Gaussian fitting (i.e., fitted peak-1 and fitted peak-2). It indicates the existence of additional phase that possesses overlapped reflection with $\{110\}_{B2}$. The low-magnification electron back-scattered diffraction (EBSD) inverse pole figure (Fig. 3c) reveals that this alloy has randomly-oriented grains with the size from tens to hundreds of microns. Figure 3d displays the scanning electron microscope back-scattered electron (SEM-BSE) image and corresponding electron probe microanalyzer (EPMA) mappings of Nb6-HEA. Four kinds of phase constitutions can be identified: (i) dominant B2 matrix with dark-gray contrast in BSE image, which contributes to the strongest peak-1 in Fig. 3b; (ii) β-Nb phase with black contrast in BSE image, which is formed due to the limit solid solubility of Nb within B2 matrix; (iii) micron-sized Cu-rich phase with light-gray contrast in BSE image, which could contribute to the additional peak-2 in Fig. 3b; (iv) a very small volume fraction of Hf-rich oxide with the brightest contrast in BSE image, which is further confirmed by EPMA mapping for O (Supplementary Fig. S9). Despite that micro-scale phase segregation

https://doi.org/10.1038/s41467-025-56580-9

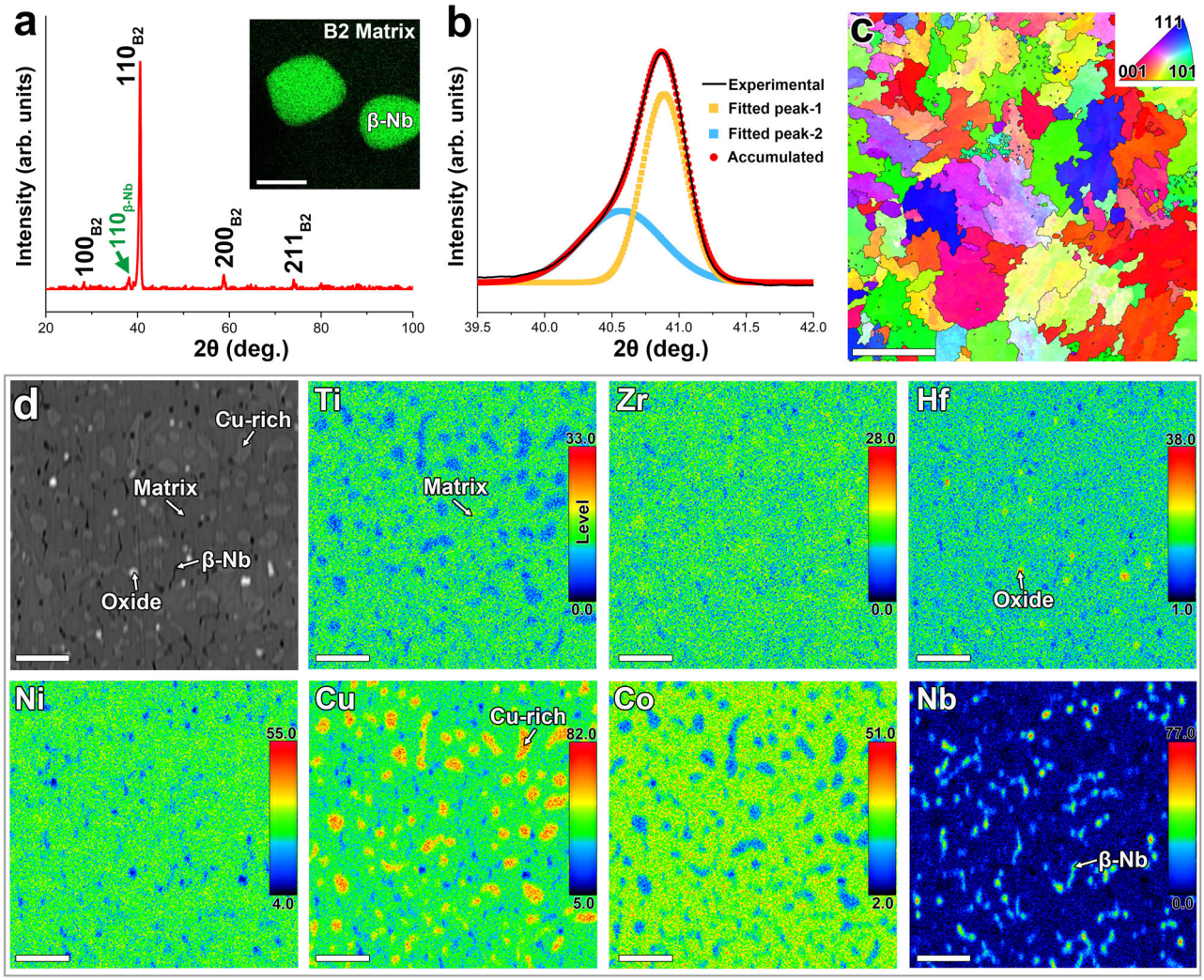

Fig. 3 | Microstructural characterizations of Nb6-HEA. a X-ray diffraction (XRD) pattern, where the inset shows energy dispersive spectrometer (EDS) mapping for Nb obtained by scanning transmission electron microscopy (STEM) (scale bar, 2 μm). **b** Step-scanned XRD pattern and corresponding fitting results, Accumulated stands for the sum of fitted peak-1 and fitted peak-2. **c** Electron backscattered diffraction (EBSD) inverse pole figure (scale bar, 200 μm). **d** Scanning electron microscope backscattered electron (SEM-BSE) image and corresponding electron probe micro-analyzer (EPMA) mappings for Ti, Zr, Hf, Ni, Cu, Co and Nb (scale bar, 10 μm).

occurs, the B2 matrix still contains all the alloying elements, thus having high mixing entropy. Consequently, the present Nb6-HEA is actually a natural composite that possesses various micron-sized structural/compositional heterogeneities throughout the B2 matrix.

Structural and compositional heterogeneities from micro- to nano-scale

Figure 4a shows the low-magnification scanning transmission electron microscopy energy dispersive X-ray spectroscopy (STEM-EDS) mapping images of Nb6-HEA, which clearly display the compositional difference between B2 matrix, Cu-rich phase, β-Nb phase and Hf-rich oxide, being consistent with the EPMA results (Fig. 3d). According to the line-scanning element analysis (Fig. 4b), the Cu-rich phase also possesses higher Zr content than the B2 matrix. Transmission electron microscopy (TEM) electron diffraction patterns taken from Cu-rich phase (Fig. 4c) and matrix phase (Fig. 4d) are identified by the orthorhombic Zr_7Cu_{10}-type structure[47] with [001] zone axis and the B2 structure with [111] zone axis, respectively. These two patterns are obtained without tilting the specimen, therefore the orientation relationship between them is [010]-Zr_7Cu_{10} // [0$\bar{1}$1]-B2 and (001)-Zr_7Cu_{10} // (111)-B2. Determined from diffraction pattern (Fig. 4c), the Zr_7Cu_{10}-type phase has lattice parameters of $a = 1.222$ nm and $b = 0.914$ nm, which are slightly smaller than those of standard Zr_7Cu_{10} structure[47] due to the existence of Ni and Co with smaller atomic radii than Cu. Then, the fitted peak-2 in Fig. 3b could be attributed to the {422} reflection of Zr_7Cu_{10}-type phase. Further analysis shows that the Cu-rich region also contains the orthorhombic Zr_3Cu_8-type phase with low volume fraction (Supplementary Fig. S10), and a similar behavior of phase decomposition (coexistence of Zr_7Cu_{10} and Zr_3Cu_8 intermetallics) has been previously reported in Zr-Cu alloy[48]. Notably, the diffraction pattern taken within B2 matrix (Fig. 4d) exhibits weak and diffused superlattice spots at 1/2{101}* and 1/2{224}* positions (indicated by blue and yellow arrows). These 1/2 spots have been previously observed in the defects-bearing Ti-Ni alloys with strain glass transition, which result from the appearance of B19′ nano-domains[49]. Figure 4e shows the TEM bright-field image taken within B2 matrix of Nb6-HEA, where nano-domains with dark contrasts can be observed. The filtered high-resolution transmission electron microscopy (HRTEM) image (Fig. 4f) displays one typical nano-domain with B19′ structure (identified by the inset Fast Fourier transform (FFT) pattern), which possesses distinct atomic arrangement from surrounding B2 matrix. We have also prepared a Nb-free $(TiZrHf)_{50}Ni_{25}Cu_{15}Co_{10}$ HEA (named as the Nb0-HEA), which exhibits a typical B2 → B19′ martensitic transformation[23]. Unlike the Nb6-HEA containing B19′ nano-domains,

https://doi.org/10.1038/s41467-025-56580-9

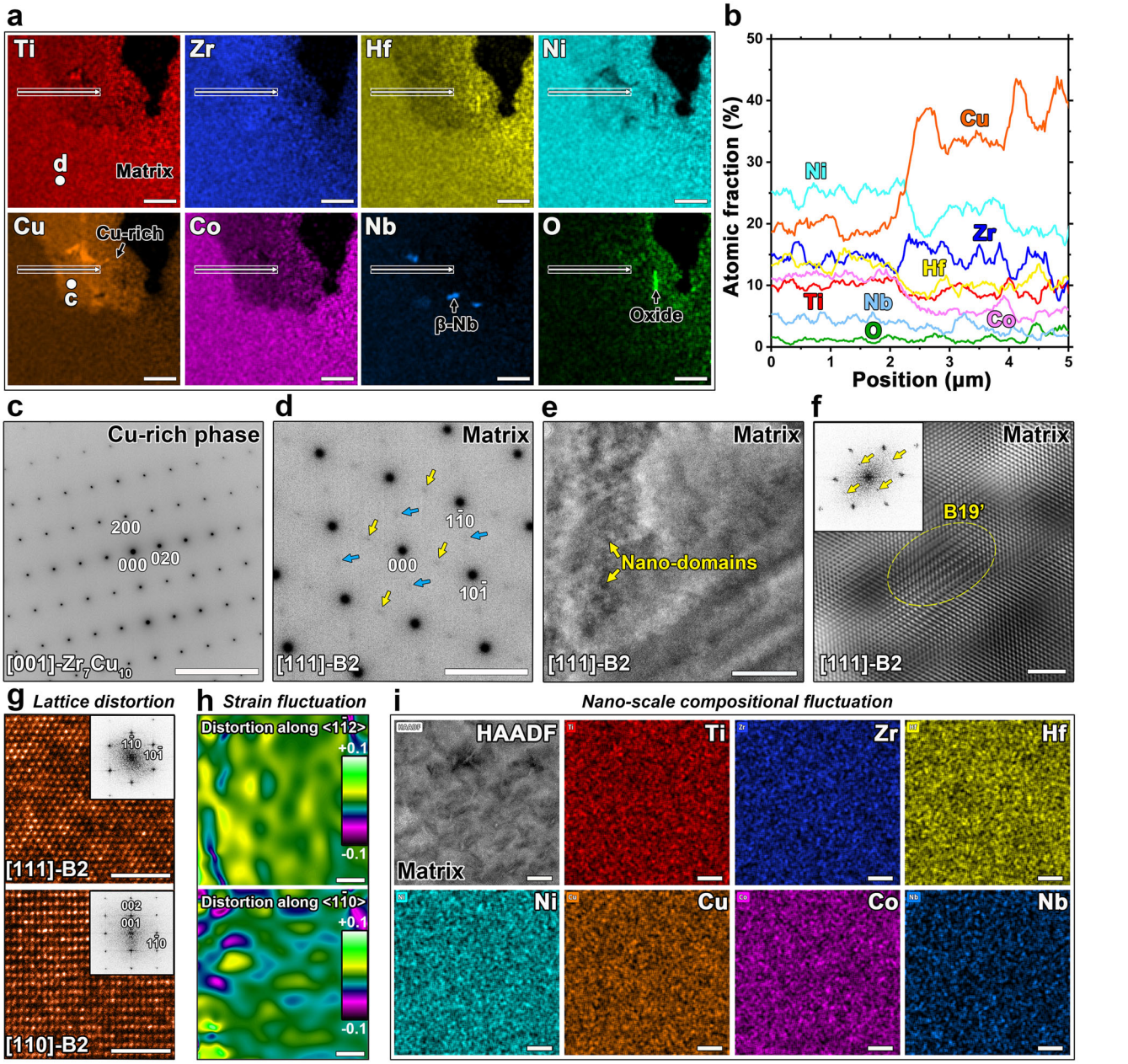

Fig. 4 | Structural and compositional analysis of Nb6-HEA. a Low-magnification scanning transmission electron microscopy energy dispersive X-ray spectroscopy (STEM-EDS) mappings for Ti, Zr, Hf, Ni, Cu, Co, Nb and O (scale bar, 2 μm). **b** Line-scanning element analysis recorded along the white line in (**a**). **c** Transmission electron microscopy (TEM) electron diffraction pattern taken within the Cu-rich phase in **a**, which is indexed by the orthorhombic Zr_7Cu_{10} structure with [001] zone axis (scale bar, 5 nm^{-1}). **d** TEM electron diffraction pattern taken within the matrix in (**a**), which is indexed by the cubic B2 structure with [111] zone axis, where the superlattice reflections for B19′ variants are indicated by yellow and blue arrows respectively (scale bar, 5 nm^{-1}). **e** TEM bright-field image taken within B2 matrix, showing heterogeneous micromorphology (scale bar, 100 nm). **f** Filtered high-resolution transmission electron microscopy (HRTEM) image that displays one B19′ nano-domain within B2 matrix (scale bar, 2 nm), and the inset shows the corresponding Fast Fourier transform (FFT) pattern. **g** HRTEM images of B2 matrix taken along [110]-B2 zone axis and [111]-B2 zone axis (scale bar, 2 nm), where the insets show the corresponding FFT patterns. **h** Geometry phase analysis (GPA) images that display local strain distribution along $<1\bar{1}2>_{B2}$ direction and $<1\bar{1}0>_{B2}$ direction (scale bar, 2 nm). **i** High-angle annular dark-field (HAADF) image taken within B2 matrix and corresponding high-magnification STEM-EDS mappings for Ti, Zr, Hf, Ni, Cu, Co and Nb (scale bar, 50 nm).

micron-sized B19′ martensitic variants have been observed in Nb0-HEA (Supplementary Fig. S11). Thus, it seems that the long-range strain ordering will be suppressed by extra Nb doping.

Owing to the composition-induced atomic size mismatch[50], HEA systems always suffer severely local lattice distortion (i.e., atoms deviated from their ideal lattice site). In most B2 regions of Nb6-HEA, local lattice distortion can be observed, as shown in the HRTEM images taken along [110]- and [111]-B2 zone axes (Fig. 4g). The strong intensity of {001} superlattice reflections in the inset FFT image confirms the high degree of B2 ordering of matrix. And geometry phase analysis (GPA, Fig. 4h) shows the local strain distribution within B2 matrix, exhibiting intense strain fluctuation at nano-scale. High-magnification STEM-EDS mapping images (Fig. 4i) show that the B2 matrix also suffers nano-scale compositional fluctuation that has been commonly observed in HEA systems[51], and the Nb element displays a heterogeneous network-like distribution throughout B2 matrix. Interestingly, the B19′ nano-domains in Nb6-HEA will not grow into large martensitic lath even at cryogenic temperature (e.g., at 123 K, Supplementary

https://doi.org/10.1038/s41467-025-56580-9

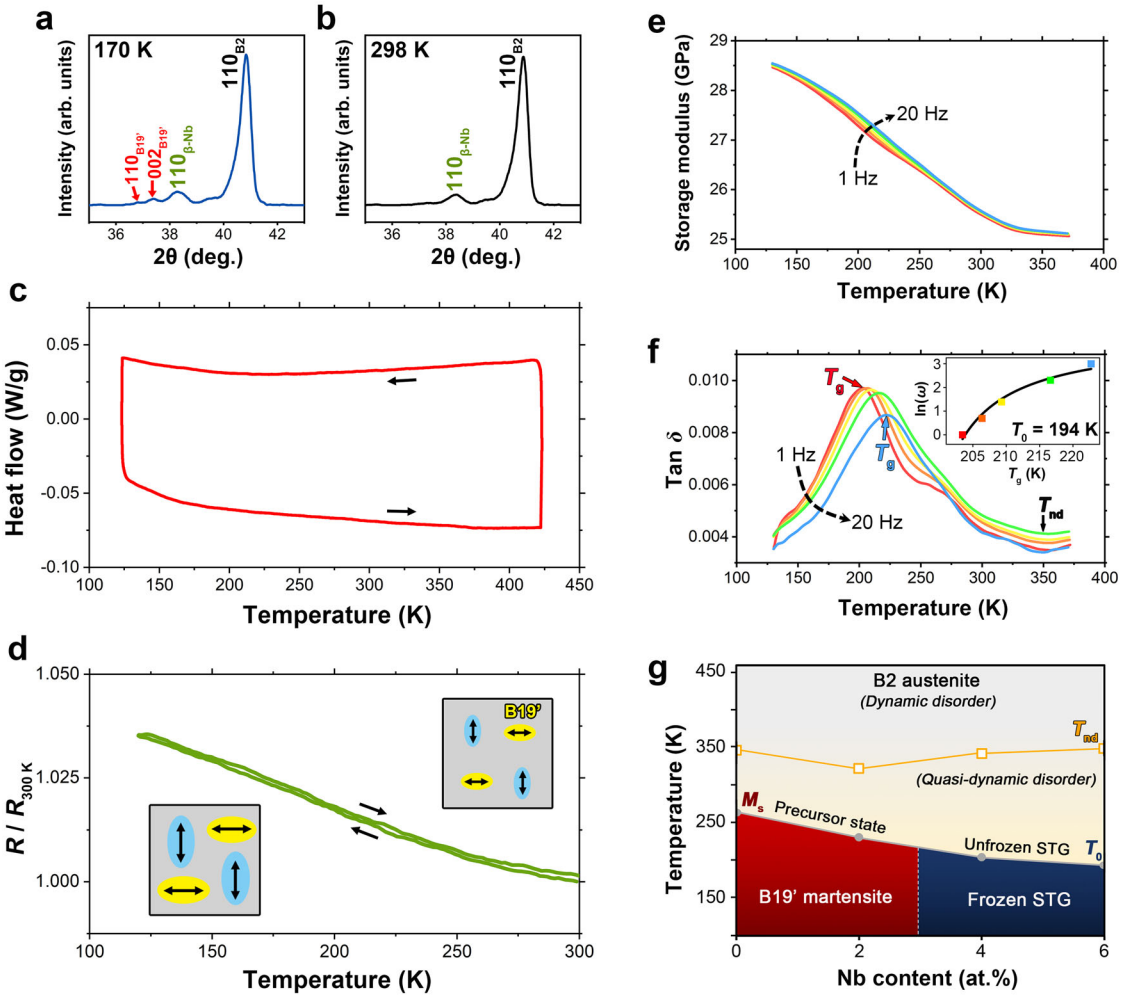

Fig. 5 | Signatures of strain glass transition in Nb6-HEA. a, **b** In-situ step-scanned XRD patterns of Nb6-HEA, taken at 170 K (**a**) and 298 K (**b**). **c** Differential scanning calorimetry (DSC) curve of Nb6-HEA, showing the absence of martensitic transformation peak. **d** Normalized (at 300 K) electrical resistivity curve of Nb6-HEA for both cooling and heating, and the insets schematically illustrate the evolution of B19′ nano-domains with temperature. **e**, **f** Frequency-dependent (different colours represent frequency of 1, 2, 4, 10 and 20 Hz, respectively) storage modulus (**e**) and internal friction tan δ (**f**, δ is the phase difference between stress and strain) obtained by dynamical mechanical analysis (DMA) measurements, where the internal friction peaks follow the Vogel-Fulcher relation with an ideal freezing temperature $T_0 = 194$ K (inset of **f**). **g** Schematic transition diagram for the B2 austenite in present HEA system, showing that doping of excess Nb can alter the martensitic transformation into strain glass transition, where M_s stands for martensitic transformation start temperature, T_g stands for peak temperature of internal friction, and STG stands for strain glass.

Fig. S12), which indicates that this alloy is not a typical martensitic alloy like the Nb0-HEA. In the following, we shall show that the present Nb6-HEA is actually a strain glass alloy, possessing the short-range strain ordering over a wide temperature range.

Trace of short-range strain ordered glass transition

As revealed by the in-situ step-scanned XRD patterns of Nb6-HEA (Fig. 5a and b), very weak {110} and {002} reflections for the monoclinic B19′ structure can be detected at 170 K, and these reflections become nearly invisible when heating to 298 K. Meanwhile, the fundamental reflections for the parent phase (e.g., $\{110\}_{B2}$) keep nearly unchanged. Notably, differential scanning calorimetry (DSC) curve (Fig. 5c) reveals no signature for typical martensitic transformation in Nb6-HEA, because the transformation latent heat is absent. These results suggest that this alloy suffers a local symmetry breaking from B2 to B19′. Notably, unlike conventional metallic materials, the electrical resistivity of Nb6-HEA shows abnormal temperature dependence that gradually increases with temperature decreasing, as shown in Fig. 5d. In the martensitic Nb0-HEA, its electrical resistivity increases rapidly when cooling to the martensitic transformation start temperature M_s (Supplementary Fig. S13). It indicates that the B19′ martensite possesses higher electrical resistivity than the B2 austenite in present HEA system. Thus, the abnormal temperature-dependence of electrical resistivity in Nb6-HEA can be attributed to the increased volume fraction of B19′ nano-domains with upon cooling, as schematically illustrated in the inset of Fig. 5d. Notably, the cooling and heating electrical resistivity curves of Nb6-HEA are smooth and nearly overlapped, unlike those of martensitic Nb0-HEA showing sharp change and large hysteresis (also see Supplementary Fig. S13). It indicates that the evolution of B19′ nano-domains in Nb6-HEA is continuous and nearly non-hysteretic. Moreover, dynamical mechanical analysis (DMA) reveals that both the storage modulus and internal friction (tan δ) of Nb6-HEA are frequency dependent, as shown in Fig. 5e and f. Unlike the martensitic Nb0-HEA having frequency-independent internal friction peaks (Supplementary Fig. 14), the internal friction peaks of Nb6-HEA show obviously frequency-dependent, which is a typical signature of a strain glass transition that has been widely observed in the Ti-Ni strain glass alloys[52]. According to previous investigations[53], the temperature T_{nd} at which

https://doi.org/10.1038/s41467-025-56580-9

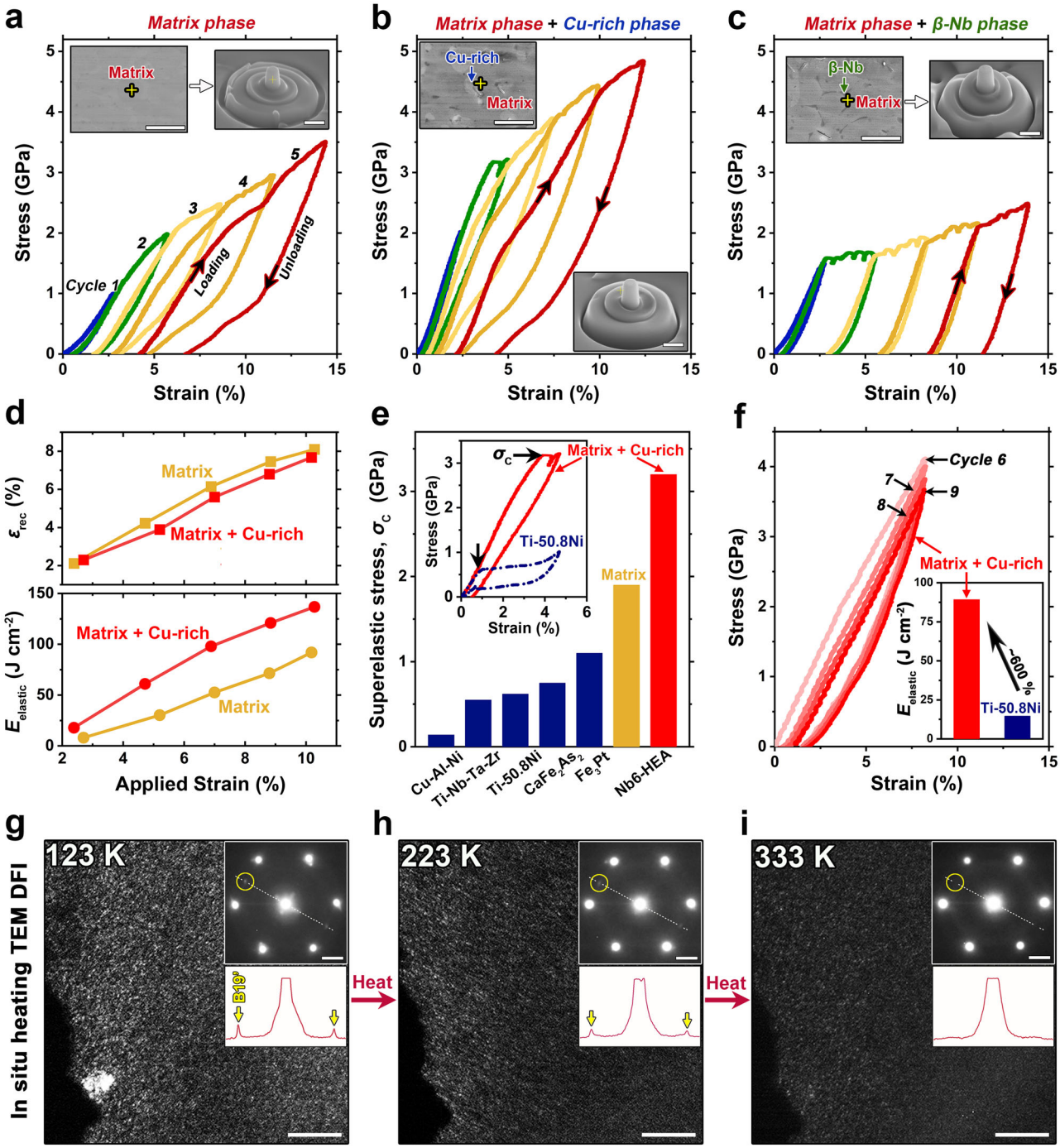

Fig. 6 | On the mechanism of superelasticity of Nb6-HEA. a–c Room-temperature cyclic compressive stress-strain curves of Nb6-HEA micropillars which consist of single matrix phase (**a**), mixture of matrix and Cu-rich phases (**b**), mixture of matrix and β-Nb phases (**c**), and "*1, 2, 3, 4, 5*" represent the number of loading-unloading cycles. The inset scanning electron microscope backscattered electron (SEM-BSE) images (scale bar, 5 μm) show the selected areas for the corresponding micropillars fabricated by the focused ion beam (FIB) milling, which are indicated by the yellow crosshairs. The inset scanning electron microscope secondary electron (SEM-SE) images (scale bar, 1 μm) show the morphology of the corresponding micropillars. **d** $\varepsilon_E + \varepsilon_{SE}$ and elastic energy $E_{elastic}$ as a function of applied strain for the "Matrix" micropillar and the "Matrix + Cu-rich" micropillar. **e** A comparison of superelastic stress σ_C between the "Matrix" micropillar, the "Matrix + Cu-rich" micropillar and previously-reported SMA micropillars[32,55–58]. The inset shows the loading-unloading stress-strain curves of the "Matrix + Cu-rich" micropillar and the Ti-50.8Ni micropillar[32] by applying strain of about 4.7%. **f** Compressive loading-unloading stress-strain curves of the "Matrix + Cu-rich" micropillar from cycle 6 to cycle 9, and the inset reveals that $E_{elastic}$ for "Matrix + Cu-rich" micropillar is 6 times of that for Ti-50.8Ni micropillar[32]. **g–i** In-situ heating TEM dark-field images (DFIs, scale bar, 50 nm) taken at 123 K (**g**), 223 K (**h**), 333 K (**i**), which are obtained by capturing one 1/2 spot belong to the B19′ structure (indicated by yellow circles), and the insets show the corresponding TEM electron diffraction patterns with [111]-B2 zone axes taken at 123 K, 223 K, 333 K respectively (scale bar, 2 nm^{-1}), and intensity profiles recorded along the dotted white lines in corresponding diffraction patterns.

internal friction starts to increase signals the appearance of quasi-static strain nano-domains (i.e., unfrozen strain glass), and the internal friction peak temperature T_g represents the freezing temperature of strain glass. The frequency-dependent T_g also follows the Vogel-Fulcher relation[53]:

$$\omega = \omega_0 \cdot \exp[-E_a/k_B(T_g - T_0)] \quad (1)$$

where E_a is the activation energy, k_B is the Boltzmann constant, and $T_0 = 194$ K is the idea strain glass freezing temperature (determined in the inset of Fig. 5f). The above features reveal that the Nb6-HEA is not a typical martensitic alloy, but a strain glass alloy. A schematic transition diagram for the B2 austenite in present HEA system is provided in Fig. 5g, which demonstrates that doping of excess Nb can alter the long-range strain ordered martensitic transformation into short-range strain ordered strain glass transition.

Discussion

Next, we shall discuss why these multi-scale structural and compositional heterogeneities result in exceptional macroscopic properties in the present Nb6-HEA.

First, to correlate the microstructure of Nb6-HEA with its macroscopic superelastic property, we have prepared micropillars with different phase constitutions, and investigated their cyclic compressive stress-strain responses, as shown in Fig. 6a–c. To avoid the influence of crystallographic anisotropy, all the micropillars were taken from adjacent regions within the same grain, and their corresponding morphology before and after mechanical testing are shown in Supplementary Fig. S15. As shown in Fig. 6a, the "Matrix" micropillar (consisting of single matrix phase) possesses σ_C of 1.9 GPa at room temperature, much higher than the coarse crystalline Ti-50.8Ni micropillar (σ_C is about 0.41 GPa)[32] and the nanocrystalline Ti-50.9Ni micropillar (σ_C is about 0.6 GPa)[54]. It suggests that the nano-scale heterogeneities within the matrix phase, including the local lattice distortion, strain and compositional fluctuations (Fig. 4g–i), can suppress the stress-induced martensitic transformation (SIMT) efficiently, hence giving rise to high σ_C. As shown in Fig. 6b, an ultrahigh σ_C of 3.2 GPa has been achieved in the "Matrix + Cu-rich" micropillar (consisting of the mixture of matrix and Cu-rich phases), about 68.4% higher than that in the "Matrix" micropillar. This dual-phase micropillar shows a small plastic deformation of 0.74% under a high applied stress of 3.9 GPa. By contrast, the "Matrix" micropillar suffers a larger plastic deformation of 1.3% under a lower applied stress of 2 GPa. These results indicate that the non-transforming Cu-rich phase, which has ultrahigh yield strength σ_y of 5.4 GPa (Supplementary Fig. S15b), can not only suppress the SIMT, but also impede the dislocation glide in surround matrix phase. As shown in Fig. 6c, the "Matrix + β-Nb" micropillar (consisting of the mixture of matrix and β-Nb phases) shows σ_y of 1.6 GPa and negligible superelasticity. The superelasticity absence can be attributed to that the β-Nb phase has suffered severely plastic deformation before reaching σ_C (1.9 GPa) of matrix phase. Therefore, the β-Nb phase cannot provide prominent strengthening effect at room temperature. However, with temperature decreasing, σ_C of matrix phase will become lower than 1.6 GPa at a critical temperature due to the Clausius-Clapeyron relation[14], and the β-Nb phase can then be considered as a strengthening phase which plays a role like the Cu-rich phase. In addition, the non-transforming β-Nb phase can act as the obstacles for thermally-induced/stress-induced long-range strain ordering. As shown in Fig. 6d, with the same applied strain, the "Matrix + Cu-rich" micropillar possesses smaller $\varepsilon_E + \varepsilon_{SE}$ than the "Matrix" one due to its lower volume fraction of transforming component, whereas possesses much superior capability for elastic energy storage owing to its higher applied stress. In comparison with previously-reported SMA micropillars[32,55–58] (Fig. 6e), the "Matrix + Cu-rich" micropillar possesses much higher σ_C, which may have potential applications in superelastic micro-devices. Moreover, the "Matrix + Cu-rich" micropillar maintains high $E_{elastic}$ after several loading-unloading cycles, which is nearly 6 times of the Ti-50.8Ni micropillar[32], as shown in Fig. 6f. Consequently, the nano-scale heterogeneities within the matrix phase and micro-scale secondary phases can increase the barrier for SIMT cooperatively, resulting in the enhancement of σ_C, and their strengthening effects decreases the undesirable plastic deformation that deteriorates the superelasticity.

Second, the wide temperature range superelasticity of Nb6-HEA (Fig. 1) benefits from the kinetically-limited strain glass transition of B2 matrix. The micron-sized secondary phases, local lattice distortion and compositional fluctuation at nano-scale can be deemed the structural defects/random fields that help to suppress the thermally-induced martensitic transformation[17,59]. At $T_0 < T \le T_{nd}$, this alloy should contain the quasi-static strain nano-domains (i.e., unfrozen strain glass) which can serve as the embryos for the reversible SIMT. At $T \le T_0$, this alloy will fall into a frozen strain glass state with a high density of B19′ nano-domains. We have further performed in-situ TEM dark-field observations to reveal the "living" feature of B19′ nano-domains, as shown in Fig. 6g–i. At 123 K (Fig. 6g), a high density of frozen B19′ nano-domains are randomly distributed throughout the matrix, which do not grow into large martensitic laths. When heating to 223 K (Fig. 6h), both size and volume fraction of B19′ nano-domains decrease smoothly, which can be reflected by the weakened 1/2 spots in the inset diffraction pattern. At 333 K (Fig. 6i), the 1/2 spots are nearly invisible, and the volume fraction of B19′ nano-domains is low. The inset intensity profiles can also reveal the evolution of B19′ nano-domains upon heating. Consequently, the suppression of thermally-induced martensitic transformation in present Nb6-HEA helps to widen the temperature range for superelasticity[6,12,17].

Third, the weak temperature dependence of σ_C (Fig. 1b) of Nb6-HEA can be simply understood by the Clausius-Clapeyron relation[14]:

$$\frac{d\sigma_C}{dT} = -\frac{\triangle S}{\varepsilon \cdot V_m} \tag{2}$$

where $\triangle S$ is the molar entropy difference between the austenite and martensite, ε is the transformation strain, and V_m is the molar volume. According to a recent study[60], the maximum transformation strain, ε_{max} in the Nb0-HEA is 14.5%, much larger than that of the Ti-Ni alloy (about 8.4%)[61]. And V_m in this system is also larger than that of the Ti-Ni alloy due to the alloying of large-sized atoms. Since the Nb6-HEA processes embryonic B19′ nano-domains in a wide temperature range, the stress-induced B2 → B19′ martensitic transformation should not involve the nucleation process. The absolute value of $\triangle S$ for the growth B19′ nano-domains should be smaller than that required the complete nucleation-growth process. Therefore, owing its large εV_m and small absolute value of $\triangle S$, the Nb6-HEA exhibits a relatively weak temperature dependence of σ_C.

Fourth, the nearly temperature-independent modulus (Fig. 2a and b) of Nb6-HEA can be explained by a self-compensation effect. Upon cooling, on one hand, the lattice instability of B2 matrix will give rise to an elastic modulus softening effect, which has been usually observed at the pre-transitional state of martensitic alloys and unfrozen state of strain glass alloys[8,52]; on the other hand, the thermally-induced weakness of anharmonic phonon vibration in non-transforming secondary phases (e.g., β-Nb precipitates and Cu-rich intermetallics) will lead to an ever-present elastic modulus hardening effect[9]. Thus, a compensation effect can be established between the B2 matrix and non-transforming secondary phases, and consequently results in the desired temperature-independent elastic modulus. A schematic illustration of the mechanism for the Elinvar effect in this alloy is provided in Supplementary Fig. S16.

Fifth, the stress hysteresis of superelasticity in present Nb6-HEA varies with temperature (Fig. 1a). Such cooling-enlarged hysteresis can be attributed to: (i) the lattice compatibility between stress-induced martensite (SIM) and matrix phase becomes worsen, in other word, the middle eigenvalue λ_2 of the transformation stretch matrix is away from 1[62]; (ii) the volume fraction of SIM increases[63]; (iii) the resistance to the motion of interface between SIM and matrix phase becomes weaker[64]; (iv) the difference in free energy between SIM and matrix phase increases[65]. Technologically, large stress hysteresis should be avoided, because it will not only lead to low efficiency and inaccurate position

control of SMA actuators, but also produce fatigue damage and low durability of cardiovascular stents[6]. Actually, the stress hysteresis of present Nb6-HEA is much smaller than many landmark SMAs, e.g., Ti-50.6Ni alloy[8] and Fe-Co-Ni-Al-Ta-B alloy[10]. Using the coefficient of energy dissipation ($\delta = E_{dissipated} / (E_{elastic} + E_{dissipated})$)[64] to quantify the hysteresis of superelasticity—the higher δ is, the larger hysteresis a SMA possesses, one can find that the Nb6-HEA has much lower δ than the Nb-free $(TiZrHf)_{50}Ni_{25}Co_{20}Cu_5$ HEA (Supplementary Fig. S17). Besides, the temperature dependence of δ (i.e., $-\Delta\delta/\Delta T$) is 6.72×10^{-4} K^{-1} for Nb6-HEA, only half of that for $(TiZrHf)_{50}Ni_{25}Co_{20}Cu_5$ (13.84×10^{-4} K^{-1}). It suggests that doping Nb element in the present HEA system can effectively reduce the stress hysteresis and weaken its temperature dependence simultaneously. Since the stress hysteresis is correlated with the applied stress, one can reduce the stress hysteresis of Nb6-HEA by decreasing the applied stress magnitude. As shown in Fig. 2b, by applying an external stress of 600 MPa, this alloy exhibits non-hysteretic stress-strain response and thermally-stable elastic energy over a wide temperature range. Moreover, our experiments showed that further isothermal aging (e.g., at 723 K for 1.5 h) can also reduce the stress hysteresis of Nb6-HEA, accompanying by an obvious enhancement of σ_C (Supplementary Fig. S18), which could be attributed to the aging-induced precipitation of secondary phase, like that observed in the aged Ti-Ni alloys[8,25].

Sixth, we will discuss the roles of Nb element in the present HEA system: (i) owing to the limited solid solubility of B2 matrix, the excess Nb doping will lead to the precipitation of β-Nb as strengthening phase at low temperatures; (ii) since Nb element usually acts as the austensite-stabilizer in Ti-based alloy[66], the Nb element dissolved in B2 matrix can act as point defects that can not only suppress the long-range strain ordered martensitic transformation, but also give rise to the solid strengthening effect. In addition, the configuration entropy of mixing, ΔS_{mix}^{conf} for B2 matrix could be increased by the solute of Nb element, according to an applicable model for the multi-component B2-ordered structure[67]:

$$\Delta S_{mix}^{conf} = -\frac{R}{2}\sum_{i=1}^{n}\{x_i(1+\eta_i)\ln[x_i(1+\eta_i)] + x_i(1-\eta_i)\ln[x_i(1-\eta_i)]\} \quad (3)$$

where R is the ideal gas constant, x_i is the molar fraction concentration of the i^{th} element, n is the total number of element species, and η_i is the site-ordering parameter of the i^{th} element, which ranges from -1 to 1; (iii) the solute of Nb element can also increase the atomic size mismatch and the degree of local lattice distortion δ, according to:

$$\delta = 100\sqrt{\sum_{i=1}^{n} c_i\left(1-\frac{r_i}{\bar{r}}\right)^2} \quad (4)$$

where c_i and r_i are the atomic percentage and atomic radius of the individual alloy component respectively, $\bar{r}$ (i.e., $\sum_{i=1}^{n} c_i r_i$) is the average atomic radius, and n is the total number of element species[50]. The increased local lattice distortion will result in the enhancement of strengthening effect; (iv) according to the element distribution in the Nb-free Nb0-HEA (Supplementary Fig. S19), doping of Nb at the expense of reducing Ti, Zr and Hf content will facilitate the formation of Cu-rich intermetallics, which helps to enhance the yield strength and suppress the long-range strain ordered martensitic transformation. As a result, the Nb6-HEA possesses much superior superelastic performance to the Nb0-HEA (Supplementary Fig. S20).

Finally, it is noticed that the strain ordered nano-domains in stain glass Nb6-HEA share similarities with the polar nano-regions (PNRs) in relaxor ferroelectrics[68], both of which originate from a gradual freezing process of the disordered ferroic state[17]. These ferroic nano-regions can be detected below a critical temperature—T_{nd} for the strain glass Nb6-HEA (Figs. 5f and 6g–i) and T_B (i.e., Burns temperature) for the relaxor ferroelectrics. Around the freezing temperature, the internal fraction peaks of stain glass Nb6-HEA show a strong frequency dependence, following the Vogel-Fulcher relation (Fig. 5f). Similar behavior has been observed for ac dielectric response in relaxor ferroelectrics[69]. Unlike the traditional ferroelectrics with large ferroelectric domains, in relaxor ferroelectrics, the gradual expanding and contracting of PNRs under external electric field can give rise to remarkable electromechanical properties, e.g., large electrostriction with slim hysteresis[69]. Such electromechanical response is very like the "smoothed" (or "quasi-linear") stress-strain response in Nb6-HEA (Fig. 1a). Considering the physical parallelism between strain glass and relaxor, it can be deemed that the strain ordered nano-domains in Nb6-HEA can also evolve gradually under external stress field, contributing to large superelasticity with slim hysteresis[6]. Very recently, a high-entropy relaxor ferroelectric has been developed, showing high recoverable energy density and efficiency[70]. Therefore, the high-configuration-entropy strategy is not only applicable in exploiting relaxor ferroelectrics with excellent properties, but also feasible in achieving high performance in the physically-parallel ferroelastic systems.

In summary, we report a $(TiZrHf)_{44}Ni_{25}Cu_{15}Co_{10}Nb_6$ high-entropy superelastic alloy, which is a natural composite that bears the highly-distorted B2 matrix phase and various structural and compositional heterogeneities from micron- to nano-scale. Owing to the unique microstructure, the matrix suffers short strain ordering (strain glass transition), for which the thermally-induced long-range strain ordering (martensitic transformation) as hindered by the multi-scale heterogeneities. These heterogeneities also provide high energy barrier against the dislocation movements, thus giving rise to a significant strengthening effect. And their ever-present elastic modulus hardening effect cancels out the elastic modulus softening effect of transformative matrix. As a result, this alloy exhibits an exceptional combination of wide-temperature-range high superelastic stress, large elastic recovery strain, and Elinvar effect. Our work may provide an appealing elastic material serving in temperature-variable environments like space and aerospace, as well as a promising candidate for industrial applications, such as leaf springs in automobiles, mechanical chronometers and high-precision devices.

Methods

Sample preparation

$(TiZrHf)_{50-x}Ni_{25}Cu_{15}Co_{10}Nb_x$ (x = 0, 2, 4, 6 at.%) and $(TiZrHf)_{50}Ni_{25}Co_{20}Co_5$ ingots were prepared by arc-melting furnace under a protective argon atmosphere, using raw materials with high purity (Ti: 99.995 at.%, Zr: 99.5 at.%, Hf: 99.95 at.%, Ni: 99.995 at.%, Co: 99.95 at.%, Cu: 99.99 at.% and Nb: 99.95 at.%). The ingots were turned over and melted five times to ensure homogeneity. Then, the as-cast ingots were followed by annealing at 1273 K for 3 h in a quartz tube with argon atmosphere, and quenched into water. Samples were cut from the center of quenched ingots, and then mechanically polished for the following measurements and characterizations. Several $(TiZrHf)_{44}Ni_{25}Cu_{15}Co_{10}Nb_6$ (Nb6-HEA) samples were further isothermal aging at 723 K for 1.5 h for reducing the stress hysteresis, or exposing to 373 K for 10 days (i.e., 240 h) for examining the stability at its upper temperature limit. Commercial Ti-Ni50 alloy and GB 65Mn spring steel were used for comparison.

Mechanical testing

Cylinder samples with size of Φ4 mm × 7 mm were used to obtain the compressive superelastic response, using the LD26 (Lishi) universal testing machine equipped with the extensometer (Epsilon 3541), with the loading rate of 0.13 mm/min and unloading rate of 0.5 mm/min. Different cylinder samples were used to measure the superelastic response at each temperature. Dog-bone samples with gauge dimension of (6 mm × 1.8 mm × 1.2 mm) were used to obtain the tensile stress-strain curves, using the AG-IS (Shimadzu) universal testing

machine equipped with the extensometer (Epsilon 3442), with the loading and unloading rates of 0.1 mm/min. The microhardness test was evaluated by a Vickers hardness tester HV-1000 STA (Veiyee) at a load of 2.942 N for 15 s. The hardness was determined by the average of the five testing points.

Cycling stability testing

Cylinder samples with size of Φ3 mm × 8 mm were used to obtain the cyclic compressive stress-strain curves (100 cycles), using the LD26 (Lishi) universal testing machine equipped with the extensometer (Epsilon 3541), with the loading and unloading rates of 3 mm/min. Different cylinder samples were used to measure the cyclic performance at each temperature. Room-temperature compressive fatigue tests were performed by the material testing machine EHF-U (Shimadzu), under a constant stress amplitude of 1.6 GPa with frequency of 3 Hz. Dog-bone samples with gauge dimension of (6 mm × 1.8 mm × 1.2 mm) were used to obtain the room-temperature cyclic tensile stress-strain curves, using the CMT4204 (Chenxin) universal testing machine, with the loading and unloading rates of 3 mm/min.

Electrochemical corrosion testing

Potential polarization curves were obtained by the CHI660E electrochemical analyzer system (Chenhua), in a conventional three-electrode cell with environments of 3.5 wt.% NaCl and H_2SO_4 (PH = 3) respectively. Calomel electrode (SCE) and Pt electrode were used as the reference electrode and counter electrode, respectively. The testing area for Nb6-HEA in 3.5 wt.% NaCl solution was 2.31 cm^2, for Nb6-HEA in H_2SO_4 (PH = 3) solution was 2.34 cm^2, for Ti-50Ni alloy in 3.5 wt.% NaCl solution was 2.45 cm^2, for Ti-50Ni alloy in H_2SO_4 (PH = 3) solution was 1.85 cm^2.

Micropillar compression testing

Micropillars with different phase constitutions were prepared by a scanning electron microscope equipped with a focus ion beam (FIB-SEM, FEI Scios 2). All micropillars were taken from the same grain of matrix phase. The size for "Matrix" micropillar was Φ0.513 μm × 1.041 μm, for "Matrix + Cu-rich" micropillar was Φ0.524 μm × 1.311 μm, for "Cu-rich" micropillar was Φ0.544 μm × 1.213 μm and for "Matrix + β-Nb" micropillar was Φ0.533 μm × 1.082 μm. Room-temperature micropillar compression was performed by the FIB-SEM equipped with picoindenter Hysitron PI 85, using the loading and unloading rates of 5 nm/s.

Structural and compositional analysis

Average structure was identified using X-ray diffraction (XRD, XRD-7000 Shimadzu) with Cu Kα radiation, using the samples with size of 10 mm × 10 mm × 1 mm. Electron back-scattered diffraction (EBSD) characterization was conducted by the JSM 7200 F SEM equipped with the EDAX Velocity Super detector. Scanning electron microscope backscattered electron (SEM-BSE) images and electron probe microanalyzer (EPMA) mappings were performed by the JXA-iHP200F. Transmission electron microscope (TEM) foil samples with diameter of 3 mm were prepared by twin-jet electropolishing at temperatures below 243 K, followed by short-term ion milling to remove surface contamination. Microstructure and elemental distribution were characterized using the 200 kV JEOL JEM-2100F TEM and the Thermo Fisher Talos F200S TEM. In-situ TEM observations were performed by the 200 kV JEOL JEM-2100F TEM. High-resolution TEM images and geometric phase analysis (GPA) were analyzed using DigitalMicrograph software (3.2 version, Gatan).

Characterization of strain glass transition

Temperature-dependent electrical resistivity was measured using physical property measurement system (PPMS, Quantum Design) with cooling and heating rates of 2 K/min, using the samples with size of 7.5 mm × 3 mm × 0.8 mm. Differential scanning calorimetry (DSC) experiment was carried out using the TA DSC Q-200 with cooling and heating rates of 5 K/min, using the samples with size of 1.5 mm × 1.5 mm × 1.5 mm. Dynamical mechanical analyzer (DMA, TA Q-850) was employed to measure the temperature-dependent storage modulus and internal friction at 1 Hz, 2 Hz, 4 Hz, 10 Hz and 20 Hz, under the single cantilever mode with cooling rate of 5 K/min and strain amplitude of 0.05%, and using the samples with size of 10 mm × 4 mm × 0.8 mm.

Data availability

The data that support the findings of this study are available in the Figshare database (https://doi.org/10.6084/m9.figshare.27151434). Source data are provided with this paper.

References

1. He, Q. et al. A highly distorted ultraelastic chemically complex Elinvar alloy. *Nature* **602**, 251–257 (2022).
2. Duerig, T. W. Present and future applications of shape memory and superelastic materials. *Proc. MRS* **360**, 497–506 (1994).
3. Jani, J. M., Leary, M., Subic, A. & Gibson, M. A. A review of shape memory alloy research, applications and opportunities. *Mater. Des.* **56**, 1078–1113 (2014).
4. Zhang, C. et al. Strong and ductile FeNiCoAl-based high-entropy alloys for cryogenic to elevated temperature multifunctional applications. *Acta Mater* **242**, 118449 (2023).
5. Liu, C. et al. A lightweight strain glass alloy showing nearly temperature-independent low modulus and high strength. *Nat. Mater.* **21**, 1003–1007 (2022).
6. Wang, D. et al. Superelasticity of slim hysteresis over a wide temperature range by nanodomains of martensite. *Acta Mater* **66**, 349–359 (2014).
7. Otsuka, K. & Wayman, C. M. *Shape Memory Materials* (Cambridge Univ. Press, Cambridge, 1999).
8. Otsuka, K. & Ren, X. Physical metallurgy of Ti-Ni-based shape memory alloys. *Prog. Mater. Sci.* **50**, 511–678 (2005).
9. Newnham, R. E. *Properties of Materials: Anisotropy, Symmetry, Structure* (Oxford Univ. Press, Oxford, 2004).
10. Tanaka, Y. et al. Ferrous polycrystalline shape-memory alloy showing huge superelasticity. *Science* **327**, 1488–1490 (2010).
11. Yang, S. et al. Excellent superelasticity of Cu-Al-Mn-Cr shape memory single crystal obtained only through annealing cast polycrystalline alloy. *Scr. Mater.* **165**, 20–24 (2019).
12. Xiong, C. et al. Superelasticity over a wide temperature range in metastable β-Ti shape memory alloys. *J. Alloys Compd.* **853**, 157090 (2021).
13. Tseng, L. W., Ma, J., Karaman, I., Wang, S. J. & Chumlyakov, Y. I. Superelastic response of the FeNiCoAlTi single crystals under tension and compression. *Scr. Mater.* **101**, 1–4 (2015).
14. Wollants, P., De Bonte, M. & Roos, J. R. A thermodynamic analysis of the stress-induced martensitic-transformation in a single-crystal. *Z. Metallkd.* **70**, 113–117 (1979).
15. Omori, T. et al. Superelastic effect in polycrystalline ferrous alloys. *Science* **333**, 68–71 (2011).
16. Odaira, T., Xu, S., Xu, X., Omori, T. & Kainuma, R. Elastocaloric switching effect induced by reentrant martensitic transformation. *Appl. Phys. Rev.* **7**, 031406 (2020).
17. Ji, Y. et al. Ferroic glasses. *npj Comput. Mater.* **3**, 43 (2017).
18. Chen, H. et al. Unprecedented non-hysteretic superelasticity of [001]-oriented NiCoFeGa single crystals. *Nat. Mater.* **19**, 712–718 (2020).
19. Dang, P. et al. Cryogenic superelasticity and elastocaloric effect in a nanostructured Ti-Ni-Co alloy. *Scr. Mater.* **236**, 115638 (2023).

20. Wang, L. et al. Superelastic effect in Ti-rich high entropy alloys via stress-induced martensitic transformation. *Scr. Mater.* **162**, 112–117 (2019).
21. Wang, L., Lu, W., Qin, J., Zhang, F. & Zhang, D. Texture and superelastic behavior of cold-rolled TiNbTaZr alloy. *Mater. Sci. Eng. A* **491**, 372–377 (2008).
22. Xu, S. et al. Non-Hookean large elastic deformation in bulk crystalline metals. *Nat. Commun.* **13**, 5307 (2022).
23. Yaacoub, J., Abuzaid, W., Brenne, F. & Sehitoglu, H. Superelasticity of $(TiZrHf)_{50}Ni_{25}Co_{10}Cu_{15}$ high entropy shape memory alloy. *Scr. Mater.* **186**, 43–47 (2020).
24. Li, H. et al. High tensile strength and superelasticity of directionally solidified $Ti_{30}Ni_{30}Fe_{10}Hf_{10}Nb_{20}$ eutectic high entropy alloy. *Acta Metall. Sin. (Engl. Lett.)* **35**, 1583–1590 (2022).
25. Timofeeva, E. E. et al. The superelasticity and shape memory effect in Ni-rich Ti-51.5Ni single crystals after one-step and two-step ageing. *Mater. Sci. Eng. A* **796**, 140025 (2020).
26. Wang, Y., Ren, X., Otsuka, K. & Saxena, A. Temperature-stress phase diagram of strain glass $Ti_{48.5}Ni_{51}$. *Acta Mater* **56**, 2885–2896 (2008).
27. Karaca, H. E., Karaman, I., Chumlyakov, Y. I., Lagoudas, D. C. & Zhang, X. Compressive response of a single crystalline CoNiAl shape memory alloy. *Scr. Mater.* **51**, 261–266 (2004).
28. Acar, E., Tobe, H., Kaya, I., Karaca, H. E. & Chumlyakov, Y. I. Compressive response of $Ni_{45.3}Ti_{34.7}Hf_{15}Pd_5$ and $Ni_{45.3}Ti_{29.7}Hf_{20}Pd_5$ shape-memory alloys. *J. Mater. Sci.* **50**, 1924–1934 (2015).
29. Ogawa, Y., Ando, D., Sutou, Y. & Koike, J. A lightweight shape-memory magnesium alloy. *Science* **353**, 368–370 (2016).
30. Shim, J. H. et al. Improvement in the superelasticity of a Ti-35.5Ni-15Cu (at.%) alloy using $Ti(Ni,Cu)_2$ phase. *Mater. Sci. Eng. A* **847**, 143346 (2022).
31. Wang, D. et al. Transition in superelasticity for $Ni_{55-x}Co_xFe_{18}Ga_{27}$ alloys due to strain glass transition. *EPL* **98**, 46004 (2012).
32. Hua, P., Xia, M., Onuki, Y. & Sun, Q. Nanocomposite NiTi shape memory alloy with high strength and fatigue resistance. *Nat. Nanotechnol.* **16**, 409–413 (2021).
33. Chluba, C. et al. Ultralow-fatigue shape memory alloy films. *Science* **348**, 1004–1007 (2015).
34. Strnadel, B., Ohashi, S., Ohtsuka, H., Ishihara, T. & Miyazaki, S. Cyclic stress-strain characteristics of Ti-Ni and Ti-Ni-Cu shape memory alloys. *Mater. Sci. Eng. A* **202**, 148–156 (1995).
35. Dornelas, V. M., Oliveira, S. A., Savi, M. A., Pacheco, P. M. C. L. & de Souza, L. F. G. Fatigue on shape memory alloys: Experimental observations and constitutive modeling. *Int. J. Solids Struct.* **213**, 1–24 (2021).
36. Nejezchlebová, J. et al. The effect of athermal and isothermal ω phase particles on elasticity of β-Ti single crystals. *Acta Mater* **110**, 185–191 (2016).
37. Cui, J. & Ren, X. Elinvar effect in Co-doped TiNi strain glass alloys. *Appl. Phys. Lett.* **105**, 061904 (2014).
38. Wang, W. et al. Reentrant strain glass transition in Ti-Ni-Cu shape memory alloy. *Acta Mater* **226**, 117618 (2022).
39. Torres, H., Varga, M. & Ripoll, M. R. High temperature hardness of steels and iron-based alloys. *Mater. Sci. Eng. A* **671**, 170–181 (2016).
40. Ghosh, D., Subhash, G., Radhakrishnan, R. & Sudarshan, T. S. Scratch-induced microplasticity and microcracking in zirconium diboride–silicon carbide composite. *Acta Mater* **56**, 3011–3022 (2008).
41. Odaira, T. et al. Flexible and tough superelastic Co-Cr alloys for biomedical applications. *Adv. Mater.* **34**, 2202305 (2022).
42. Nune, K. C., Misra, R. D. K., Li, S. J., Hao, Y. L. & Yang, R. Osteoblast cellular activity on low elastic modulus Ti-24Nb-4Zr-8Sn alloy. *Dent. Mater.* **33**, 152–165 (2017).
43. Prasher, M. et al. Effect of Hf solute addition on the phase transformation behavior and hardness of a Ni-rich NiTi alloy. *Mater. Chem. Phys.* **247**, 122890 (2020).
44. de Araújo, C. J., da Silva, N. J., da Silva, M. M. & Gonzalez, C. H. A comparative study of Ni-Ti and Ni-Ti-Cu shape memory alloy processed by plasma melting and injection molding. *Mater. Des.* **32**, 4925–4930 (2011).
45. Abubakar, R. A. & Nuhu, I. Application of NiTi shape memory alloy in ocean thermal energy conversion. *MRS Energy & Sustain.* **11**, 479–500 (2024).
46. Zhang, J., Chen, T., Li, W., Bednarcik, J. & Dippel, A. C. High temperature superelasticity realized in equiatomic Ti-Ni conventional shape memory alloy by severe cold rolling. *Mater. Des.* **193**, 108875 (2020).
47. Albisetti, A. F., Biffi, C. A. & Tuissi, A. Synthesis and structural analysis of $Cu_{10}Zr_7$. *J. Alloys Compd.* **544**, 42–45 (2012).
48. Wang, N., Li, C., Du, Z., Wang, F. & Zhang, W. The thermodynamic re-assessment of the Cu-Zr system. *Calphad* **30**, 461–469 (2006).
49. Liang, Q. et al. Novel B19′ strain glass with large recoverable strain. *Phys. Rev. Mater.* **1**, 033608 (2017).
50. Song, H. et al. Local lattice distortion in high-entropy alloys. *Phys. Rev. Mater.* **1**, 023404 (2017).
51. Ding, Q. et al. Tuning element distribution, structure and properties by composition in high-entropy alloys. *Nature* **574**, 223–227 (2019).
52. Sarkar, S., Ren, X. & Otsuka, K. Evidence for strain glass in the ferroelastic-martensitic system $Ti_{50-x}Ni_{50+x}$. *Phys. Rev. Lett.* **95**, 205702 (2005).
53. Wang, D. et al. Strain glass in Fe-doped Ti-Ni. *Acta Mater* **58**, 6206–6215 (2010).
54. Hua, P., Chu, K., Ren, F. & Sun, Q. Cyclic phase transformation behavior of nanocrystalline NiTi at microscale. *Acta Mater* **185**, 507–517 (2020).
55. San Juan, J., Nó, M. L. & Schuh, C. A. Superelastic cycling of Cu–Al–Ni shape memory alloy micropillars. *Acta Mater* **60**, 4093–4106 (2012).
56. Wang, L. et al. Tensile and superelastic behaviors of Ti-35Nb-2Ta-3Zr with gradient structure. *Mater. Des.* **194**, 108961 (2020).
57. Xiao, F., Chu, K., Ren, F. & Fukuda, T. Superelasticity of micropillar of single crystalline Fe_3. *Pt. Materialia* **9**, 100534 (2020).
58. Sypek, J. T. et al. Superelasticity and cryogenic linear shape memory effects of $CaFe_2As_2$. *Nat. Commun.* **8**, 1083 (2017).
59. Zheng, Y., Jiang, F., Li, L., Yang, H. & Liu, Y. Effect of ageing treatment on the transformation behaviour of Ti-50.9at. *Ni alloy. Acta Mater.* **56**, 736–745 (2008).
60. Rehman, I. U., Li, S. & Nam, T. H. Transformation behavior and superelasticity of TiZrHfNiCoCu multi-component high-temperature shape memory alloys. *J. Alloys Compd.* **884**, 161108 (2021).
61. Kudoh, Y., Tokonami, M., Miyazaki, S. & Otsuka, K. Crystal structure of the martensite in Ti-49.2 at.%Ni alloy analyzed by the single crystal X-ray diffraction method. *Acta Metall* **33**, 2049–2056 (1985).
62. Zarnetta, R. et al. Identification of quaternary shape memory alloys with near-zero thermal hysteresis and unprecedented functional stability. *Adv. Funct. Mater.* **20**, 1917–1923 (2010).
63. Toker, G. P., Saedi, S., Acar, E., Ozbulut, O. E. & Karaca, H. E. Loading frequency and temperature-dependent damping capacity of NiTiHfPd shape memory alloy. *Mech. Mater.* **150**, 103565 (2020).
64. Saedi, S., Acar, E., Raji, H., Saghaian, S. E. & Mirsayar, M. Energy damping in shape memory alloys: A review. *J. Alloys Compd.* **956**, 170286 (2023).
65. Zhang, J. et al. Stress-induced strain glass to martensite (R) transition in a $Ti_{50}Ni_{44.5}Fe_{5.5}$ alloy. *Phys. Rev. B* **83**, 174204 (2011).

66. Wang, M., Jiang, M., Liao, G., Guo, S. & Zhao, X. Martensitic transformation involved mechanical behaviors and wide hysteresis of NiTiNb shape memory alloys. *Prog. Nat. Sci. Mater.* **22**, 130–138 (2012).
67. Santodonato, L. J. et al. Deviation from high-entropy configurations in the atomic distributions of a multi-principal-element alloy. *Nat. Commun.* **6**, 5964 (2015).
68. Polinger, V. & Bersuker, I. B. Origin of polar nanoregions and relaxor properties of ferroelectrics. *Phys. Rev. B* **98**, 214102 (2018).
69. Chen, X. et al. Relaxor ferroelectric polymer exhibits ultrahigh electromechanical coupling at low electric field. *Science* **375**, 1418–1422 (2022).
70. Peng, H. et al. High-entropy relaxor ferroelectric ceramics for ultrahigh energy storage. *Nat. Commun.* **15**, 5232 (2024).

Acknowledgements

J.G. acknowledges the National Natural Science Foundation of China (Grant No.: 52301249). T.M. acknowledges the National Natural Science Foundation of China (Grant Nos.: 52471207, 52071256) as well as the National Key Research and Development Program of China (Grant No.: 2022YFB3505301). C.L. acknowledges the National Natural Science Foundation of China (Grant No.: 52301246) as well as the Science and Technology Major Project of Sichuan Province (Grant No.: 2023ZDZX0028).

Author contributions

J.G. and T.M. conceived the idea. J.G., G.L., T.M. and X.Z. designed the project. J.G., G.L. and T.Y. fabricated the samples. J.G., G.L., X.L, T.Y., Y.P., Y.Q., Y.L. and Y.C. performed experiments. All authors analyzed the results, in particular, C.L. and X.R. helped to analyze the results of strain glass transition. J.G. and T.M. wrote the manuscript with input from all authors.

Competing interests

The authors declare no competing interests.

Additional information

Supplementary information The online version contains supplementary material available at https://doi.org/10.1038/s41467-025-56580-9.

Correspondence and requests for materials should be addressed to Junming Gou or Tianyu Ma.

Peer review information *Nature Communications* thanks the anonymous reviewer(s) for their contribution to the peer review of this work. A peer review file is available.

Reprints and permissions information is available at http://www.nature.com/reprints

Publisher's note Springer Nature remains neutral with regard to jurisdictional claims in published maps and institutional affiliations.

Open Access This article is licensed under a Creative Commons Attribution-NonCommercial-NoDerivatives 4.0 International License, which permits any non-commercial use, sharing, distribution and reproduction in any medium or format, as long as you give appropriate credit to the original author(s) and the source, provide a link to the Creative Commons licence, and indicate if you modified the licensed material. You do not have permission under this licence to share adapted material derived from this article or parts of it. The images or other third party material in this article are included in the article's Creative Commons licence, unless indicated otherwise in a credit line to the material. If material is not included in the article's Creative Commons licence and your intended use is not permitted by statutory regulation or exceeds the permitted use, you will need to obtain permission directly from the copyright holder. To view a copy of this licence, visit http://creativecommons.org/licenses/by-nc-nd/4.0/.

© The Author(s) 2025